THE UNIVERSITY of EDINBURGH

Edinburgh Research Explorer

Investigating future precipitation changes over China through a high-resolution regional climate model ensemble

Citation for published version:
Guo, J, Huang, G, Wang, X, Li, Y & Lin, Q 2017, 'Investigating future precipitation changes over China through a high-resolution regional climate model ensemble', *Earth's Future*, vol. 5, no. 3, pp. 285-303. https://doi.org/10.1002/2016EF000433

Digital Object Identifier (DOI):
10.1002/2016EF000433

Link:
Link to publication record in Edinburgh Research Explorer

Document Version:
Publisher's PDF, also known as Version of record

Published In:
Earth's Future

General rights
Copyright for the publications made accessible via the Edinburgh Research Explorer is retained by the author(s) and / or other copyright owners and it is a condition of accessing these publications that users recognise and abide by the legal requirements associated with these rights.

Take down policy
The University of Edinburgh has made every reasonable effort to ensure that Edinburgh Research Explorer content complies with UK legislation. If you believe that the public display of this file breaches copyright please contact openaccess@ed.ac.uk providing details, and we will remove access to the work immediately and investigate your claim.

Download date: 04. May. 2023

AGU PUBLICATIONS

Earth's Future

RESEARCH ARTICLE
10.1002/2016EF000433

Investigating future precipitation changes over China through a high-resolution regional climate model ensemble

Junhong Guo[1], Guohe Huang[2,3], Xiuquan Wang[2], Yongping Li[4], and Qianguo Lin[1]

[1]Key Laboratory of Regional Energy and Environmental Systems Optimization, Ministry of Education, North China Electric Power University, Beijing, China , [2]Institute for Energy, Environment and Sustainable Communities, University of Regina, Regina, Saskatchewan, Canada , [3]SC Institute for Energy, Environment and Sustainability Research, North China Electric Power University, Beijing, China , [4]School of Environment, Beijing Normal University, Beijing, China

Key Points:
- Regional precipitation patterns over China in response to global warming are investigated through the PRECIS model
- The PRECIS model performs well in simulating both the spatial and temporal patterns of precipitation
- Overall precipitation is projected to increase throughout the 21st century

Corresponding authors:
G. Huang, huang@iseis.org; X. Wang, xiuquan.wang@gmail.com

Citation:
Guo, J., G. Huang, X. Wang, and Q. Lin (2017), Investigating future precipitation changes over China through a high-resolution regional climate model ensemble, *Earth's Future*, *5*, 285–303, doi:10.1002/2016EF000433.

Received 22 AUG 2016
Accepted 6 JAN 2017
Accepted article online 12 JAN 2017
Published online 5 MAR 2017

© 2017 The Authors.

This is an open access article under the terms of the Creative Commons Attribution-NonCommercial-NoDerivs License, which permits use and distribution in any medium, provided the original work is properly cited, the use is non-commercial and no modifications or adaptations are made.

Abstract Due to climate change, rising temperature around the world will have a great potential to influence the global hydrologic cycle, thus leading to substantial changes in the spatial and temporal patterns of precipitation. In this study, the effects of global warming on the regional hydrologic cycle, particularly on the spatiotemporal patterns of precipitation, over China are investigated through a high-resolution regional climate ensemble. In detail, the PRECIS regional climate modeling system is employed to simulate the regional climate over China from 1950 to 2099 with a fine resolution of 25 km, driven by the boundary conditions from a four-member HadCM3-based perturbed-physics ensemble (i.e., HadCM3Q0, Q1, Q7, and Q13) and the ECHAM5 model. Historical simulations of the PRECIS ensemble are first compared to the observations to validate its performance in capturing both the spatial and temporal patterns of precipitation. The comparisons show that the PRECIS ensemble is likely to overestimate precipitation in the south and exhibits slight dry biases in the northwest and southeast coasts of China. The projections from the PRECIS ensemble for future periods (i.e., 2020s, 2050s, and 2080s) are then analyzed to help understand how the regional characteristics of precipitation will be affected in the context of global warming. It is shown that the annual mean precipitation over China is likely to increase throughout the 21st century (i.e., by 0.078 mm/d in 2020s, 0.218 mm/d in 2050s, and 0.360 mm/d in 2080s). This may suggest that the rising temperature due to climate change will intensify the regional hydrologic cycles in China. However, apparent spatial and temporal variations are also reported in the projected precipitations from the PRECIS ensemble. For example, bigger changes in precipitation are usually observed in summer; projected precipitation changes in the southeast are apparently higher than other regions. In addition, the results show that the fluctuation range of the ensemble simulations will increase with time periods from 2020s to 2080s, indicating that the longer the projecting periods, the more uncertain the projections will be.

1. Introduction

Global warming resulting from increasing greenhouse gases is a common challenge facing humankind. Impacts from climate change, such as constant heat waves and droughts [*Meehl et al.*, 2009; *Trenberth and Fasullo*, 2012], extreme precipitation and flooding [*Lu and Ran*, 2011; *Min et al.*, 2011], destruction of the nature ecosystems [*Hughes et al.*, 2000; *Root et al.*, 2003], and human health [*Baker-Austin et al.*, 2013]. Among these risks, the uneven distribution of interannual and annual precipitation in different regions could lead to drought or flood damage to varying degrees. Thus, it is necessary to assess the potential impacts of global warming on precipitation to develop adaptation and mitigation measures against climate change.

Physically based global climate models (GCMs) provide a useful overview of possible climate scenarios, but they do not capture local details and forcings at coarse resolution, nor do they resolve climate features at the mesoscale and regional scales [*Wetterhall et al.*, 2006; *Yu et al.*, 2014]. Exploring the projected climatologically changes at a higher spatial and temporal resolution through regional climate models (RCMs) is likely to compensate for the deficiencies with GCMs. In general, there are two common RCM downscaling techniques, statistical and dynamical downscaling. Statistical downscaling applies the quantitative relationships between large-scale coarse atmospheric variables (predictors) and local weather variables (predictands) to obtain finer outcomes, even reaching the site scales. Owing to their easy conduction and low computational

expense, statistical downscaling is a widely used climate research method [*Gagnon et al.*, 2005; *Liu and Fan*, 2013; *Wang et al.*, 2013; *Zhang and Yan*, 2015]. However, a disadvantage to this techniques, is the solution is built on a number of widely known assumptions on the underlying probabilistic model, parameter stability, as well as temporal dependence which are not always satisfied in the context of climate change [*Wang et al.*, 2014a]. In other words, the established math-statistics mapping between predictors and predictands may not meet future situation by virtue of relying too much on present day climate factors. By contrast, dynamical downscaling nests fine-resolution RCMs into GCMs to better reflect local or regional details. Besides, RCMs also have similar physical processes and mechanisms as described in GCMs, so the results simulated by dynamical downscaling techniques are closer to reality. Given their benefits, dynamical downscaling techniques are popular for climate simulations and projections [*En-Tao et al.*, 2010; *Carvalho et al.*, 2011; *Wang et al.*, 2014a, 2014b, 2015; *Wang et al.*, 2016].

Complex topography and unique climate systems heighten the impacts of climate change in China, where many areas have suffered or are experiencing more than their share of natural disasters. For example, a flood in 1998 submerged homes and took the lives of many, costing $30 billion US [*Jiang et al.*, 2008; *Yu et al.*, 2009]. In contrast, millions of people experienced severe water shortages during an extended drought in south Yunnan province from 2009 to 2010, which resulted in considerable economic losses and threats to the Chinese economy [*Jiang et al.*, 2008; *Qiu*, 2010]. It is complicated and challenging to study the problem of climate change in China and many researchers have focused their analysis on climate form and change mechanisms, such as the East Asian monsoon [*Yu et al*., 2014], Arctic sea ice [*Li*, 1996], Pacific decadal oscillation [*Shen et al.*, 2006], and ENSO [*Zhang et al.*, 2014]. However, the explanative force of these studies need more credible proofs, because climate changes are hybrid and complicated. An assessment of the potential impacts of global warming and a reliable prediction of future climate change in precipitation in the context of China are needed, and then targeted public policies and measures for adaptation and mitigation against the changing climate could be particularly important [*Adger et al.*, 2005; *Wang et al.*, 2014b]. Previous studies on precipitation in China have shortcomings or defects, such as a limited region, low resolution, short period of time and more uncertainty. To improve upon previous studies, we investigate the influences of global warming on precipitation in China using a high regional model system (PRECIS) and driven by an ensemble of five different boundary conditions. First, the model's performance is validated by a comparing observation data obtained from 1961 to 1990. Then future changes in the spatial and temporal patterns of precipitation across the country are analyzed to understand the regional impacts of human-induced global warming in China.

2. Methods and Data

2.1. Regional Climate Modeling

Developed by the Met Office Hadley Centre, PRECIS is an atmosphere and land surface regional model system. PRECIS can run at two different horizontal resolutions: $0.44^\circ \times 0.44^\circ$ (~50 km) and $0.22^\circ \times 0.22^\circ$ (~25 km) at the equator of the rotated regular latitude–longitude grid. It contains 19 levels in a vertical hybrid-coordinate system to build the complex upper atmospheric system. To resolve the initialization problem, a relaxation method is applied to drive the regional model over a lateral buffer zone of eight grid cells, where the main variables such as atmospheric pressure, wind, temperature, and humidity, comprise initial lateral boundary conditions (LBCs) [*Jones et al.*, 2004]. In addition, to capture all possible ranges of projection we use a member ensemble of LBCs, including some from a HadCM3-based perturbed physics ensemble (called QUMP, denoted by HadCM3Q0-16), and one from ECHAM5 which is generated from the Max Plank Institute's fifth generation coupled ocean–atmosphere general circulation model (see http://www-pcmdi.llnl.gov/ipcc/model_documentation/ECHAM5_MPI-OM.htm) under the IPCC SRES A1B emissions scenario.

There are 17 members for the QUMP ensemble, all of which can be applied to drive PRECIS to generate a set of high-resolution regional climate simulations. The difference among QUMP members is their sensitivity against global climate change. In this study, considering the computational cost while exploring the spread of uncertainties as much as possible, we selected Q0 (unperturbed), Q1, Q7, and Q13 (perturbed) as the model's lateral boundary data to drive PRECIS. On the other hand, the land surface scheme of PRECIS employs Met Office Surface Exchange Scheme 2.2 (MOSES 2.2), which can supply surface boundary

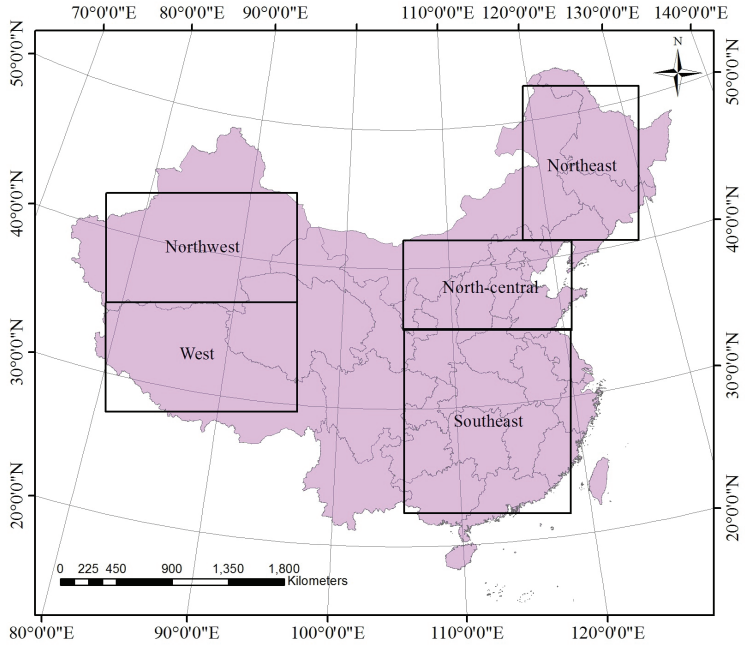

Figure 1. PRECIS model domains. There are five regions selected for validating across different climatic regions of China, which are Northeast China (NE), North-central China (NC), Southeast China (SE), West China (W), and Northwest China (NW), respectively.

Table 1. Coordinates of China Regions

No.	Region	Longitude	Latitude
1	China	66.24°E–139.48°E	10.07°N–54.34°N
2	Northeast China	117.54°N–130.17°E	40.65°N–52.29°N
3	North-central China	104.40°E–121.34°E	34.92°N–40.06°N
4	Southeast China	105.68°E–21.14°E	22.82°N–33.98°N
5	West China	78.48°E–101.16°E	30.58°N–34.84°N
6	Northwest China	75.40°E–96.39°E	37.20°N–42.22°N

conditions, such as sea-surface temperatures (SSTs), information about the extent and thickness of sea ice, and the temperature of the bottom soil layer [*Kong et al.*, 2011].

2.2. Experimental Design

The PRECIS ensemble simulations for the whole of China are carried out in a continuous run from 1949 to 2099 at a spatial resolution of 25 km, and then the time series are divided into two periods for the baseline (1961–1990) and the future (2021–2099). For the choice of study domain size, some regional selection principles are followed [*Centella-Artola et al.*, 2014] to configure a relatively reasonable domain extending from about 66.24°E–139.48°E to 10.07°N–54.34°N, which is over 38,000 25-km grid points in total. In addition, considering the internal regional features of precipitation in China and based on some previous studies [*Luo et al.*, 2013; *Yu et al.*, 2014], we select and add up to five appropriate typical samples of climatic regimes (i.e., cold, warm, wet, dry, and plateau climate) across China for the validation and undermentioned probabilistic analysis. The entire region of China and other climatic subregions are illustrated in Figure 1 and coordinates are provided in Table 1. The five subregions, which represent five distinct climate types, are the Northeast, North, Southeast, West, and Northwest of China, respectively. In addition, the simulated data from the buffer zone of eight grids and the spin-up period are removed before analysis.

2.3. Observation and Validation Methods

In this study, a gridded observational meteorological data set, derived from the Asian Precipitation-Highly-Resolved Observational Data Integration Toward Evaluation of Water Resources project in Japan (hereinafter

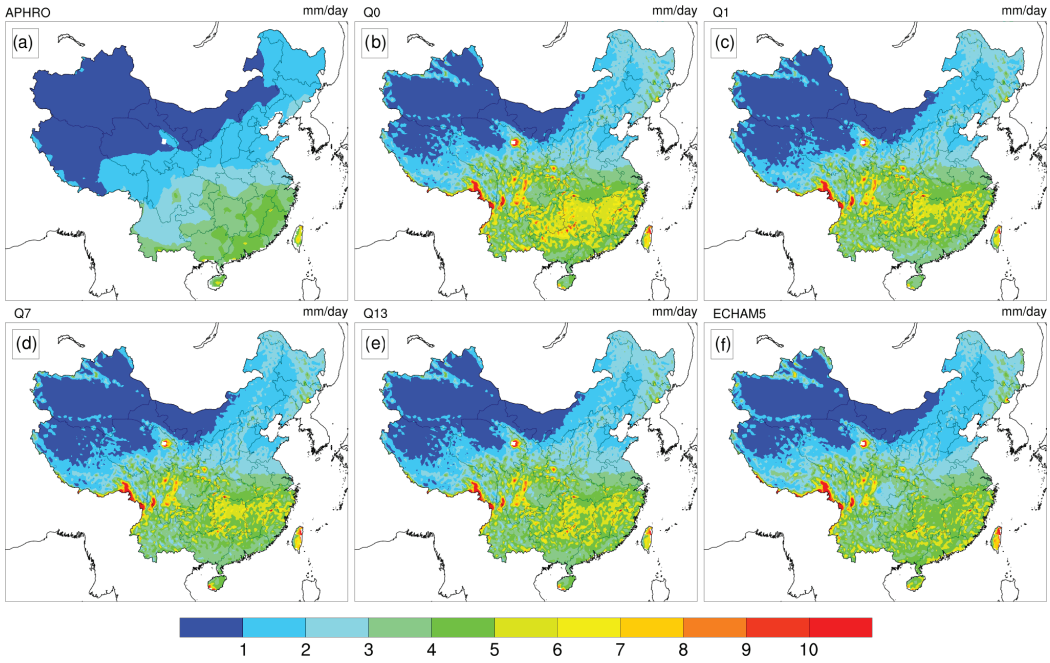

Figure 2. Comparison of (a) observed and (b–f) the simulated annual mean precipitation for China. The observations were averaged over the baseline period (1961–1990) and remapped to the same grids to compare as well as the simulations.

referred to as APHRO), is used to validate the model's ability to capture the annual and seasonal precipitation patterns. The current collection contains state-of-the-art daily gridded near-surface meteorology data (mainly precipitation and temperature) with high-resolution grids over Asia. The dataset source comes mainly from rain-gauge observation records covering a period of more than 50 years with high spatial and time resolution. Here we extract the daily gridded precipitation data subset with 0.25° daily resolution from 1961 to 1990 for the monsoon Asia domain (60°E–150°E, 15°N–55°N) as the comparison (see http://www.chikyu.ac.jp/precip/). In addition, in order to facilitate the comparison between observations and model simulations, we have regridded the simulated results to the grid cells from observational datasets.

Furthermore, to quantify the comparisons between observation and simulation, the root mean square error (RMSE) and Pearson sample linear cross-correlation coefficient (PLCC) are used to validate the model's performance, which are defined as follows:

$$\mathrm{RMSE} = \sqrt{\sum_{i=1}^{n} \frac{\left(Y_i - X_i\right)^2}{n}}, \tag{1}$$

$$\mathrm{PLCC} = \frac{\sum \left(X - \overline{X}\right)\left(Y - \overline{Y}\right)}{N\left(\sqrt{(1/n)\sum_{i=1}^{n}\left(X_i - \overline{X}\right)^2}\right)\left(\sqrt{(1/n)\sum_{i=1}^{n}\left(Y_i - \overline{Y}\right)^2}\right)}, \tag{2}$$

where X_i and Y_i represent the observed and simulated values for each cell grid, $\overline{X}$ and $\overline{Y}$ represent the mean value of observation and simulation. The two methods are used to quantify and analyze the performance of PRECIS from errors and correlation, respectively.

3. Results

3.1. Model Validation

To examine the performance of the five RCMs using PRECIS for the baseline period (1961–1990) over China, the simulations are compared with observations from annual, seasonal, and monthly precipitation in spatial and temporal scales for five subregions (i.e., NE, N, SE, W, and NW) and different seasons (i.e., DJF, MAM, JJA, and SON).

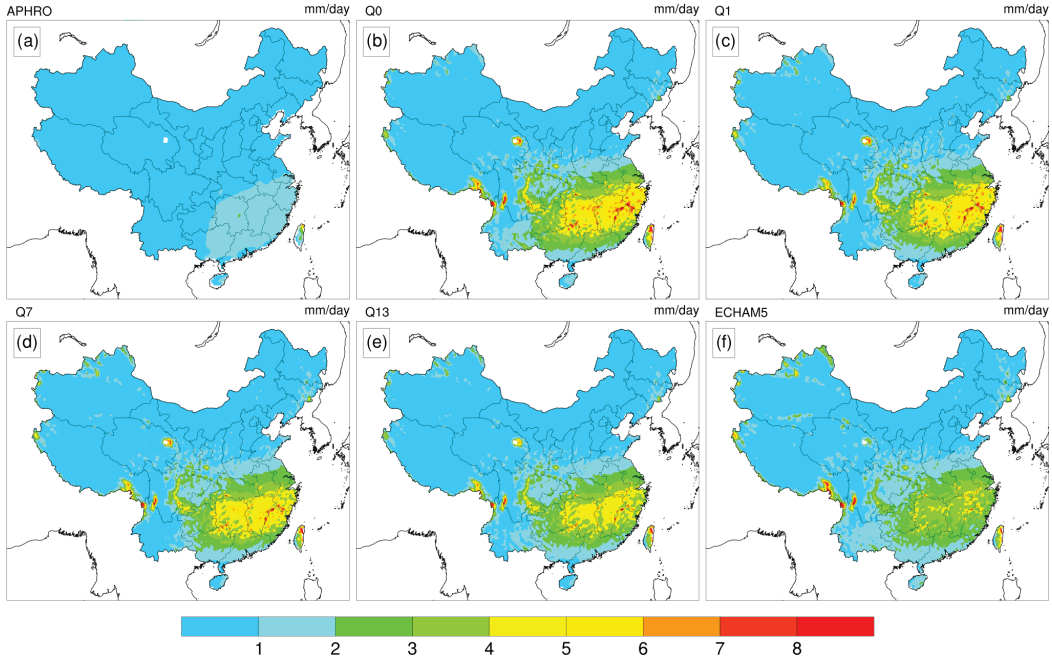

Figure 3. Comparison of (a) observed and (b–f) the simulated mean precipitation for China during DJF. The observations were averaged over the baseline period (1961–1990) and remapped to the same grids to compare as well as the simulations.

Figures 2–6 show average annual and seasonal precipitation geographic distributions in the baseline period, respectively for APHRO, Q0, Q1, Q7, Q13, and ECHAM5. Overall, the spatial patterns of precipitation suggest the models have the ability to realistically reproduce precipitation across most regions of China, although it is slightly wetter when the latitude decreases particularly in the southwest of China. In terms of both annual and seasonal comparison, the main rainfall belt of China is captured well: average precipitation increases from northwest to southeast over China, but a little bit overestimated precipitation over the south region. The dry center is located in the northwest, such as southern Xinjiang, with the annual mean precipitation less than 50 mm, while the wet center has a mean precipitation range in the southeast from 8 to 9 mm/d with the maximum precipitation in Hainan Island and Taiwan.

The precipitation simulations compare well with observations in most regions (bias of −0.5 to 0.5 mm/d). The bias of simulated average precipitation is relatively larger in the central southern China (wet bias of 3–4 mm/d) and smaller in the northwest and along Fujian-Guangdong hilly areas (dry bias of 0.5–1 mm/d) especially in spring. Five models present inconsistencies in the simulation of summer precipitation on the southeast coasts of China, for example, Q7, Q13, and ECHAM5 models show drier outcomes than others in the same regions (dry bias of 1.5 mm/d). In addition, there is a larger wet bias in winter over the southeast, while dry bias is observed in autumn in the same region.

Furthermore, among the five RCMs, QUMP ensemble models (particularly Q7) present drier biases in east China compared to ECHAM5 in summer and autumn. In spite of this, the higher sensitivity models (i.e., Q13, and ECHAM5) tend to match the magnitude of the observed winter precipitation more closely than the other three lower sensitivity models (i.e., Q0, Q1, and Q7) in the whole of China. This shows a great disagreement with others studies in which low sensitivity models have stable simulated quality (Buontempo et al. 2014).

Finally, it is noted that the simulated magnitudes of precipitation tended to significantly overestimate the observations over the Qinghai Lake and western edge of the Tibetan Plateau. The major causes for the wetter result lie in many factors. On the one hand, as the largest inland lake in China, Qinghai Lake has its own precipitation effect and is of little relevance to perimeter climate change [*Buontempo et al.*, 2014]. In addition, general climate models including PRECIS have no specific lake analysis modules or are missing some necessary boundary conditions to drive special local meteorological factors [*Williams et al.*, 2015].

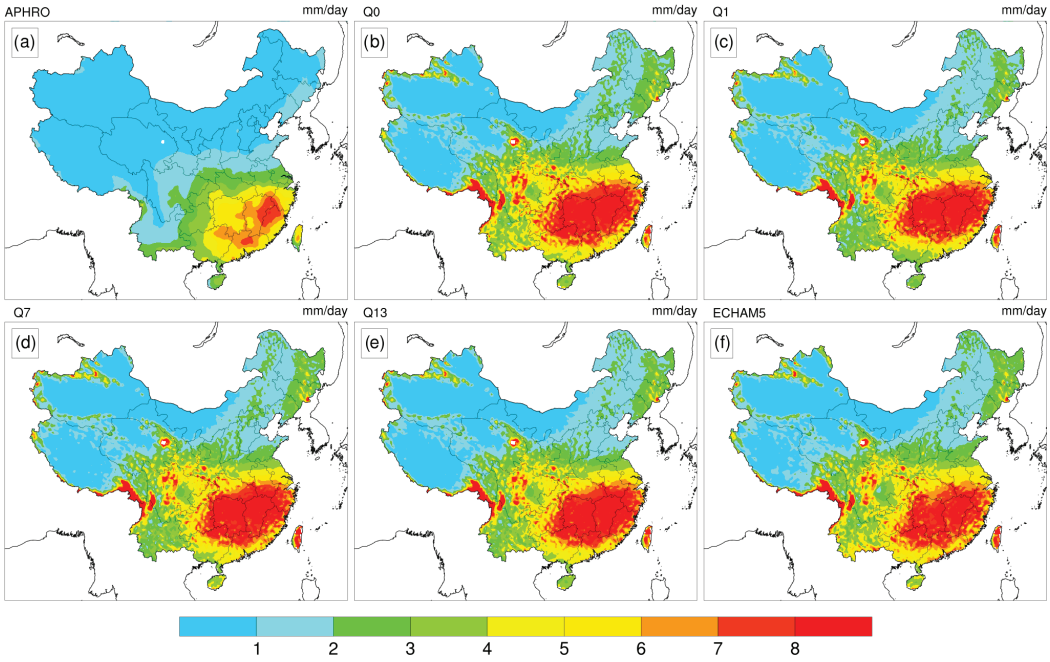

Figure 4. Comparison of (a) observed and (b–f) the simulated mean precipitation for China during MAM. The observations were averaged over the baseline period (1961–1990) and remapped to the same grids to compare as well as the simulations.

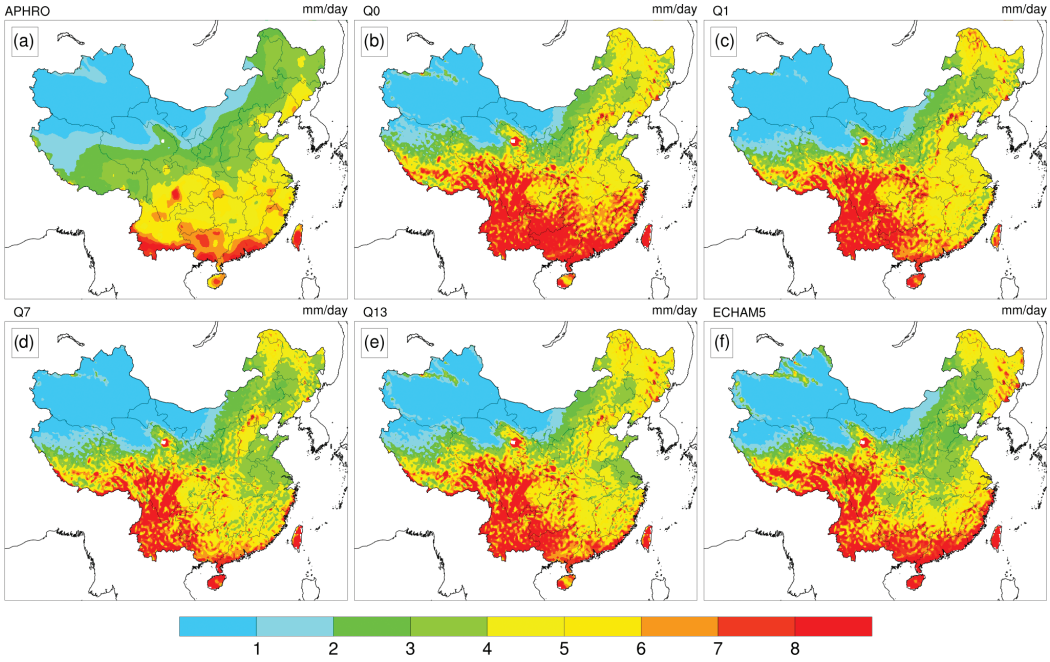

Figure 5. Comparison of (a) observed and (b–f) the simulated mean precipitation for China during JJA. The observations were averaged over the baseline period (1961–1990) and remapped to the same grids to compare as well as the simulations.

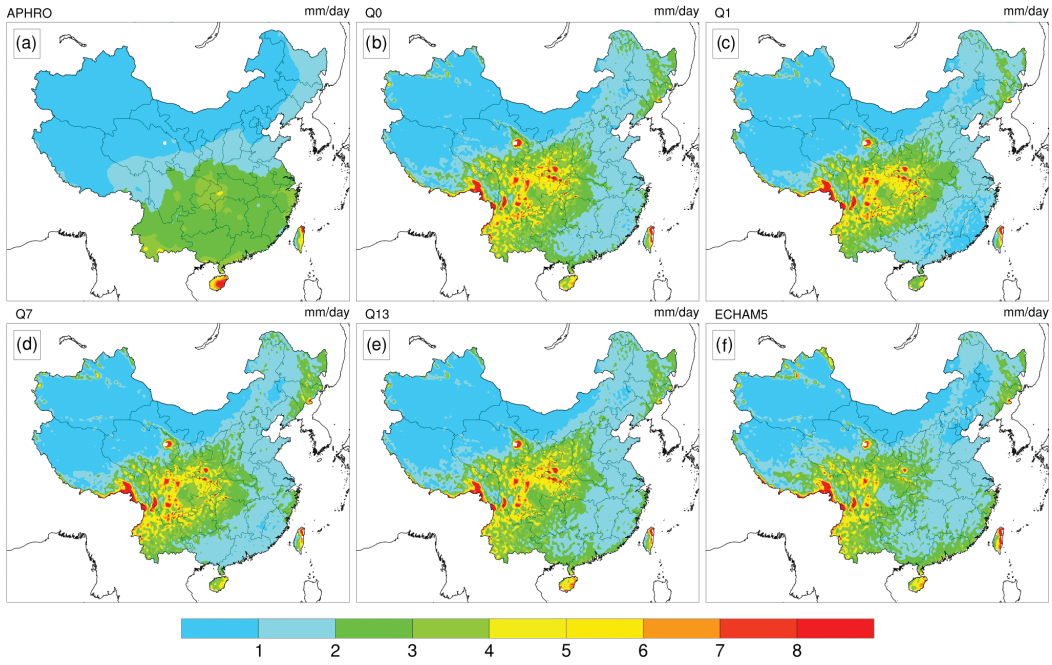

Figure 6. Comparison of (a) observed and (b–f) the simulated mean precipitation for China during SON. The observations were averaged over the baseline period (1961–1990) and remapped to the same grids to compare as well as the simulations.

Also, owing to the lack of statistical data in these remote regions, such as the plateau mountain areas, large uncertainties in climate models are unavoidable.

Figure 7 shows the comparison of the annual precipitation cycles between observations and the ensemble simulations, which are depicted by box plots (minimum, first quartile, median, third quartile, and maximum value, respectively) and averaged over the whole of China and the five divided subregions as show in Figure 1. The green line represents the mean value of five simulations and the blue line for observation. From these figures, it is generally agreed that precipitation exhibits prominent seasonal characteristics over China, for example, more precipitation in summer and less in winter whether simulations or observation, however overestimation is obvious in simulations, especially in the first half of a year. All models show less wet bias in north China (Figure 7c), where observation is within the range of simulations throughout the year, indicating that PRECIS could reasonably capture observed precipitation in that region's annual cycle. While the bias is relatively large in west especially during the rainy seasons (Figure 7e) and perhaps it also does not address the available LBC data in this region. In addition, the heaviest rainfall occurs in April instead of traditionally in summer across southeast and northwest China.

To further quantitatively analyze the model's ability in simulating the precipitation variability, we calculated the RMSE and PLCC between APHRO observation and the corresponding model simulations for annual and seasonal precipitation during the baseline period over China and the subregions (Figures 8 and 9).

The RMSE values are relatively small during autumn and winter for the whole of China, while errors are higher in the other two seasons, particularly in summer. The PLCC values of different seasons and regions are held at around 0.7, which are fairly perfect results compared with other studies [*Liu et al.*, 2013; *Luo et al.*, 2013]. For the subregions, the RMSE of the northwest is about 0.4 mm/d with a minimum of 0.319 mm/d of Q0 and the largest error occurs in the southeast (over 2.5 mm/d). The highest correlation is found in the northwest area with PLCC values around 0.8 during summer. The results suggest that the greater errors in wet regions may be attributed to a higher precipitation magnitude than arid regions [*Luo et al.*, 2013].

Generally speaking, the PRECIS ensemble performs well in capturing the spatial distribution and annual cycle of precipitation over China, although there are wet biases in the southernmost regions and slight dry biases in the northwest and southeast coasts of China in autumn. Moreover, PRECIS presents high spatial correlation in simulation against observation and small errors in autumn and winter, which also indicate it

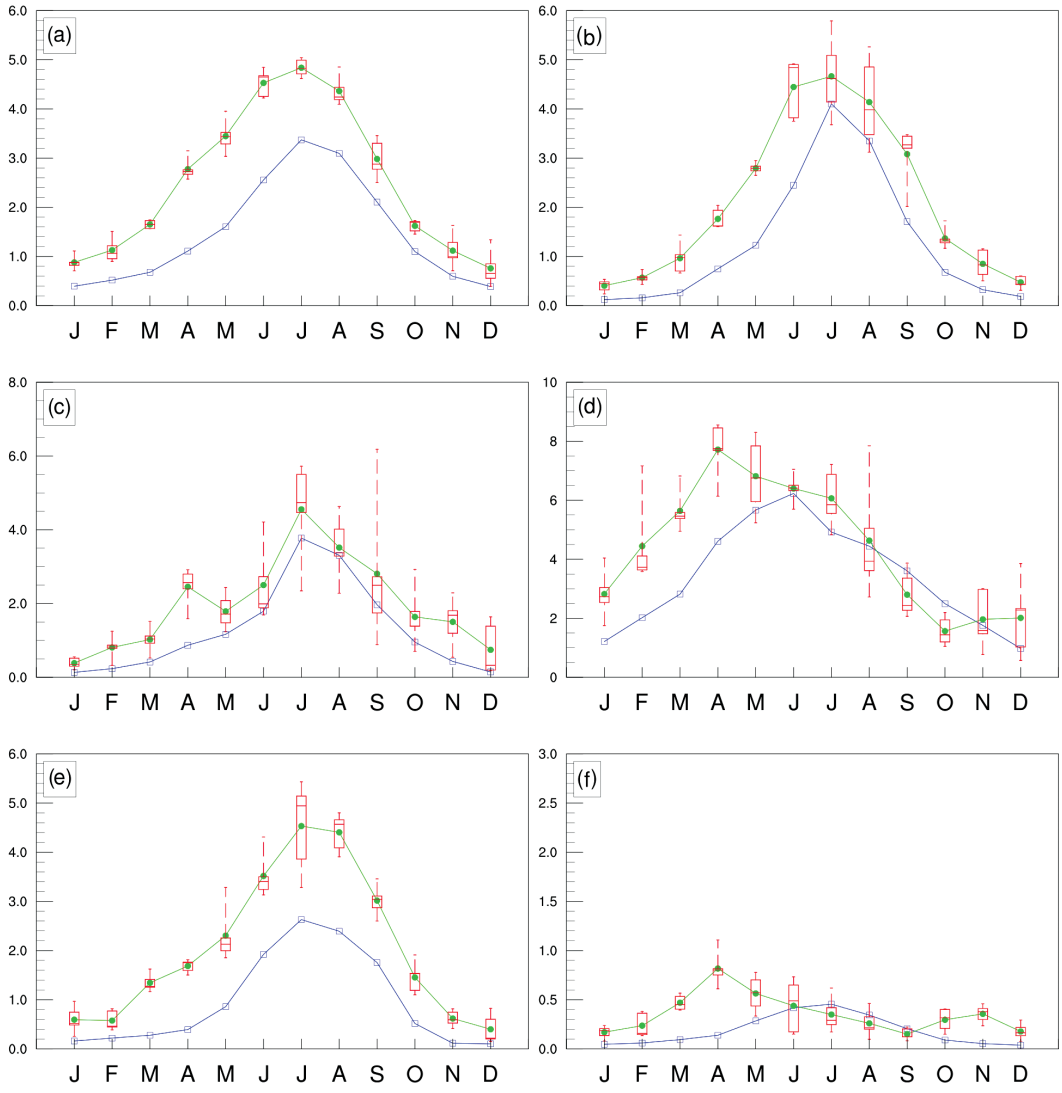

Figure 7. Annual cycles of mean precipitation (mm/d) for (a) China and (b–f) subregions during the baseline period (1961–1990). Boxes indicate the interquartile model spread (25th and 75th quantiles) with the horizontal line indicating the ensemble median and the whiskers showing the extreme range of ensemble.

can reasonably simulate the precipitation in China from another point of view. Taking into consideration of the biases, the variations of atmospheric circulation and moisture transport among models could be one reason for the question [*Yu et al.*, 2014].

3.2. Future Precipitation Projections

3.2.1. Changes in Spatial Distribution

To better analyze future precipitation trends, we divided the data into three continuous 30-year periods of the 21st century: 2011–2040 (2020s), 2041–2070 (2050s), and 2071–2099 (2080s). Figures 10–12 show the projected distributions of seasonal precipitation changes during the three periods throughout the whole of China from the five PRECIS simulations (Q0, Q1, Q7, Q13, and ECHAM5, respectively). Additionally, we also calculate each average precipitation variation for the different models in annual and seasonal scales to quantitatively describe the changes of the five subregions with the same future periods (Table 2).

Regardless of how seasons change, there is an obvious general increase in precipitation over most areas of China in the future, and all models show a similar trend in each season's spatial patterns with slight

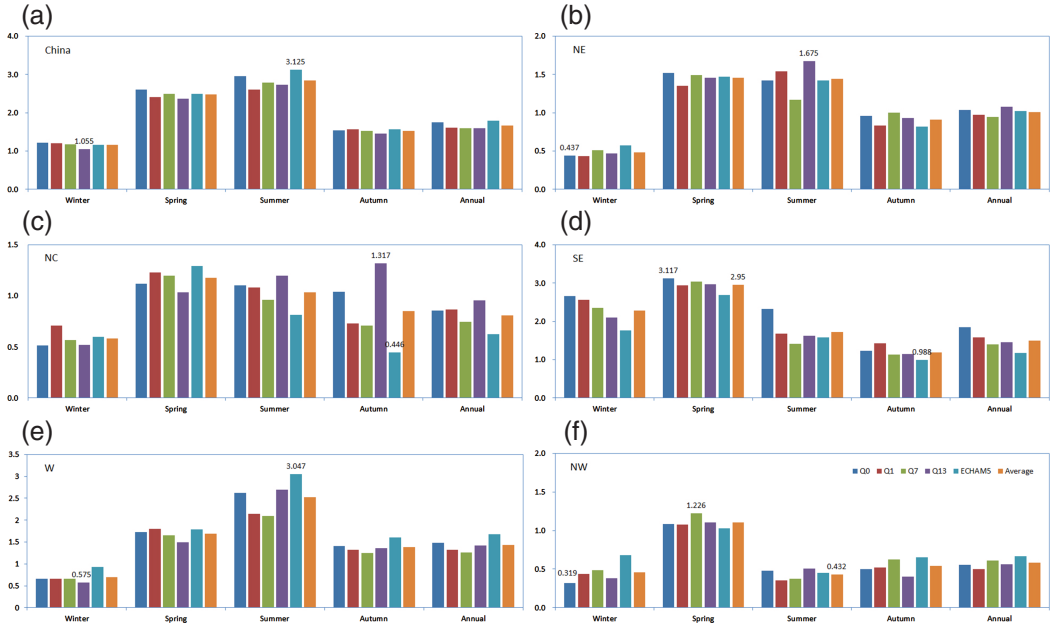

Figure 8. The root mean square error (RMSE) between observation and the ensemble for annual and seasonal precipitation over the entire China and subregions.

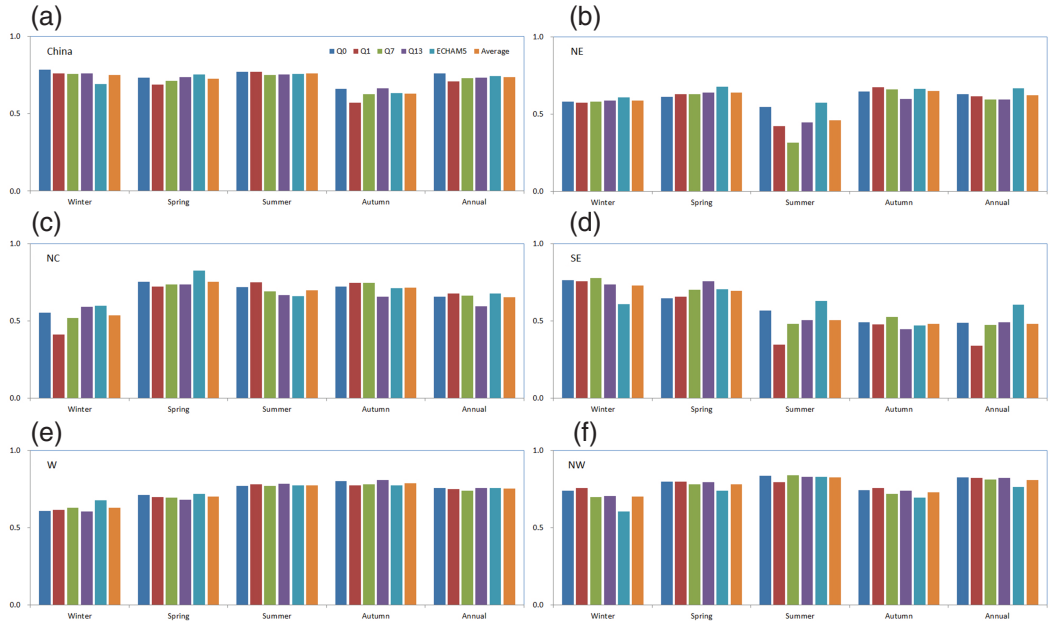

Figure 9. The Pearson sample linear cross-correlation coefficient (PLCC) between observation and the ensemble for annual and seasonal precipitation over the entire China and subregions.

differences in certain local areas. Specifically, in winter during the initial period, an increase in precipitation is found in parts of north China but reductions from 0.2 to 0.6 mm/d dominate the southeast, especially in the performance of Q0 and Q1. The pattern of rainfall increases is similar in the middle and end of the century, but has a much larger range, particularly in the southeast. It is worth noting that the QUMP ensemble is not shown in accordance with projection from ECHAM5. For example, the amount of precipitation in the south of Himalayas simulated by the QUMP ensemble is larger compared with the latter.

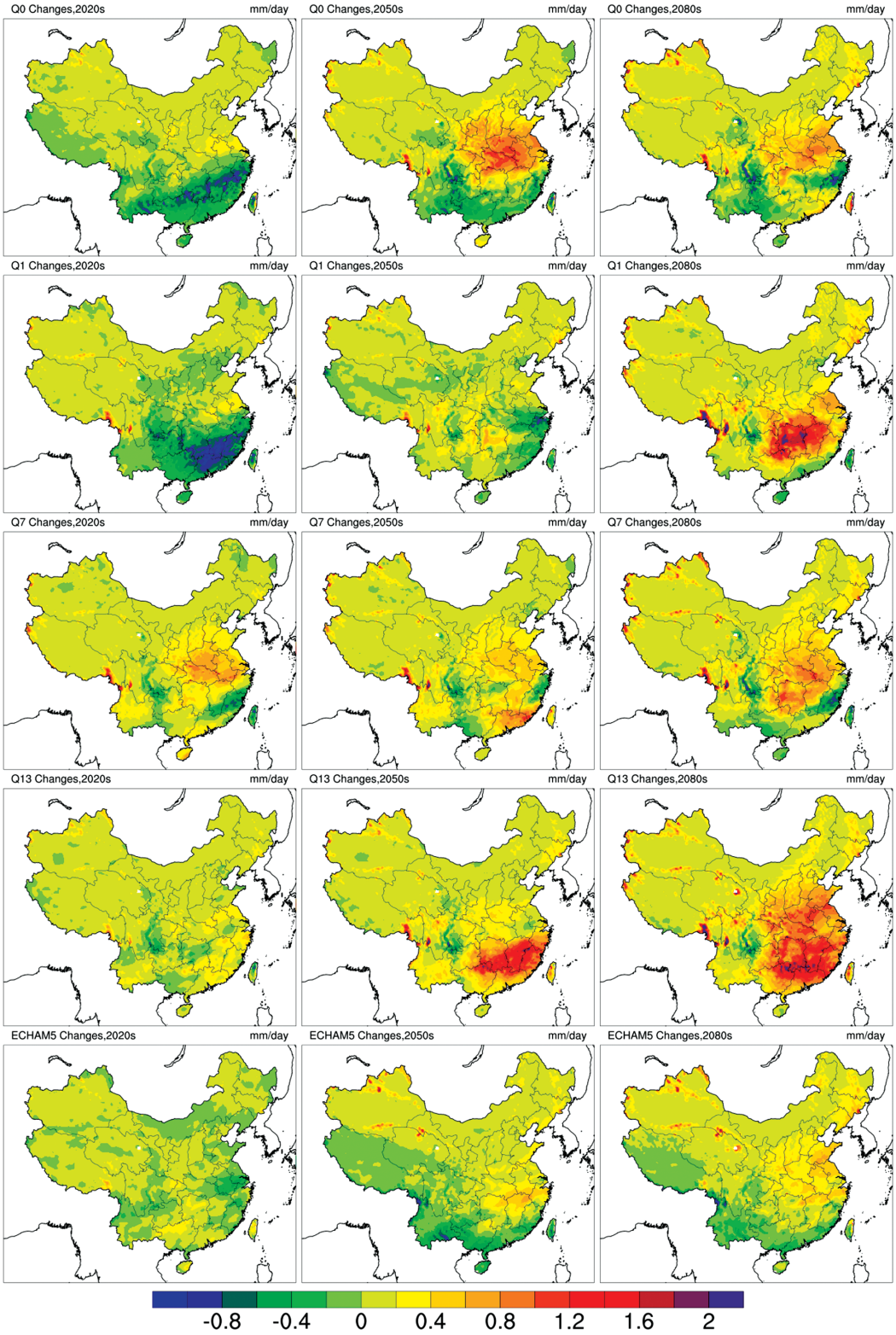

Figure 10. Projected patterns of precipitation changes (mm/d) for DJF over China in future. Each row represents an RCM member and from top to bottom these are Q0, Q1, Q7, Q13, and ECHAM5. Each column represents a period. From left to right these are 2020s, 2050s, and 2080s.

10.1002/2016EF000433

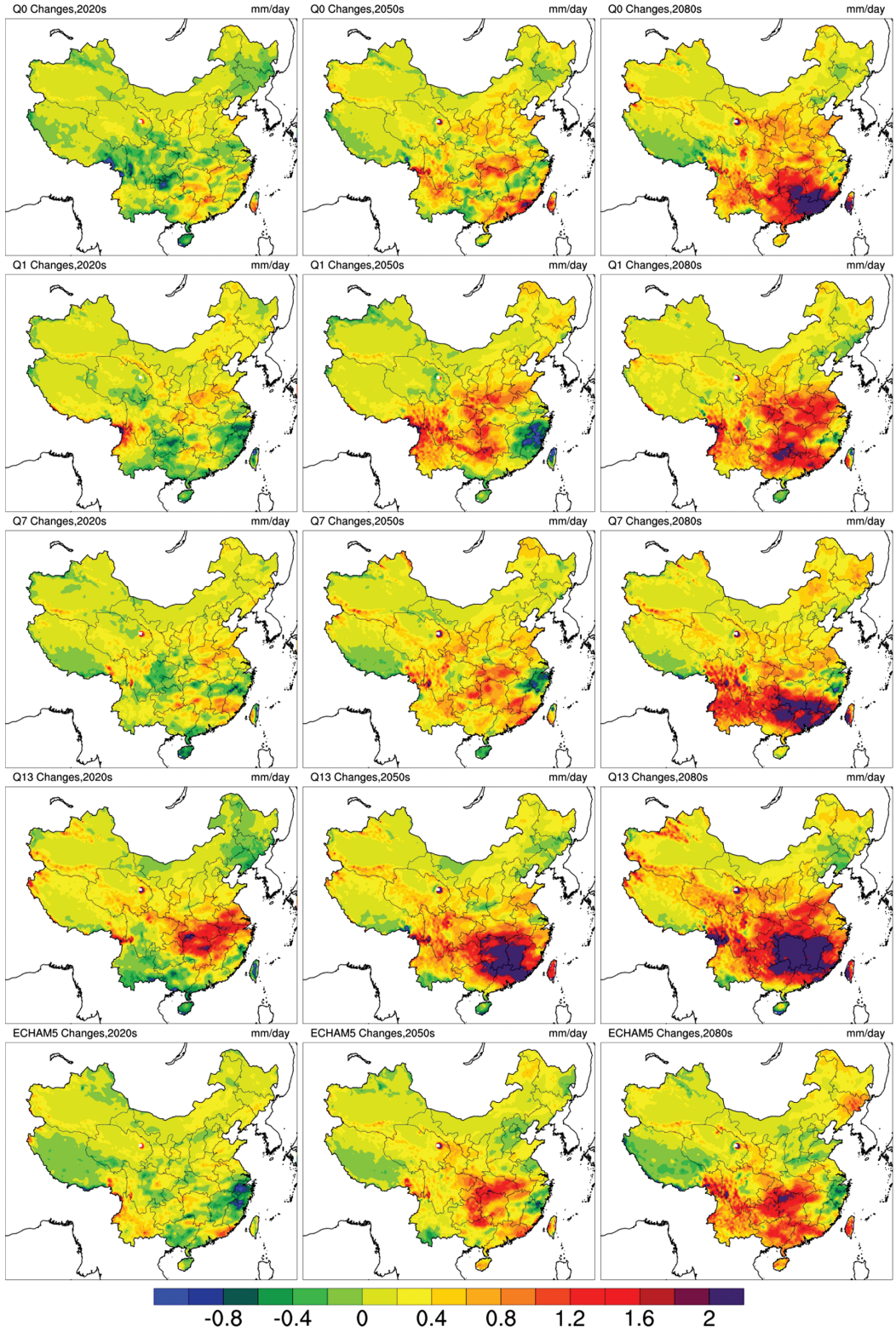

Figure 11. Projected patterns of precipitation changes (mm/d) for MAM over China in future. Each row represents an RCM member and from top to bottom these are Q0, Q1, Q7, Q13, and ECHAM5. Each column represents a period. From left to right these are 2020s, 2050s, and 2080s.

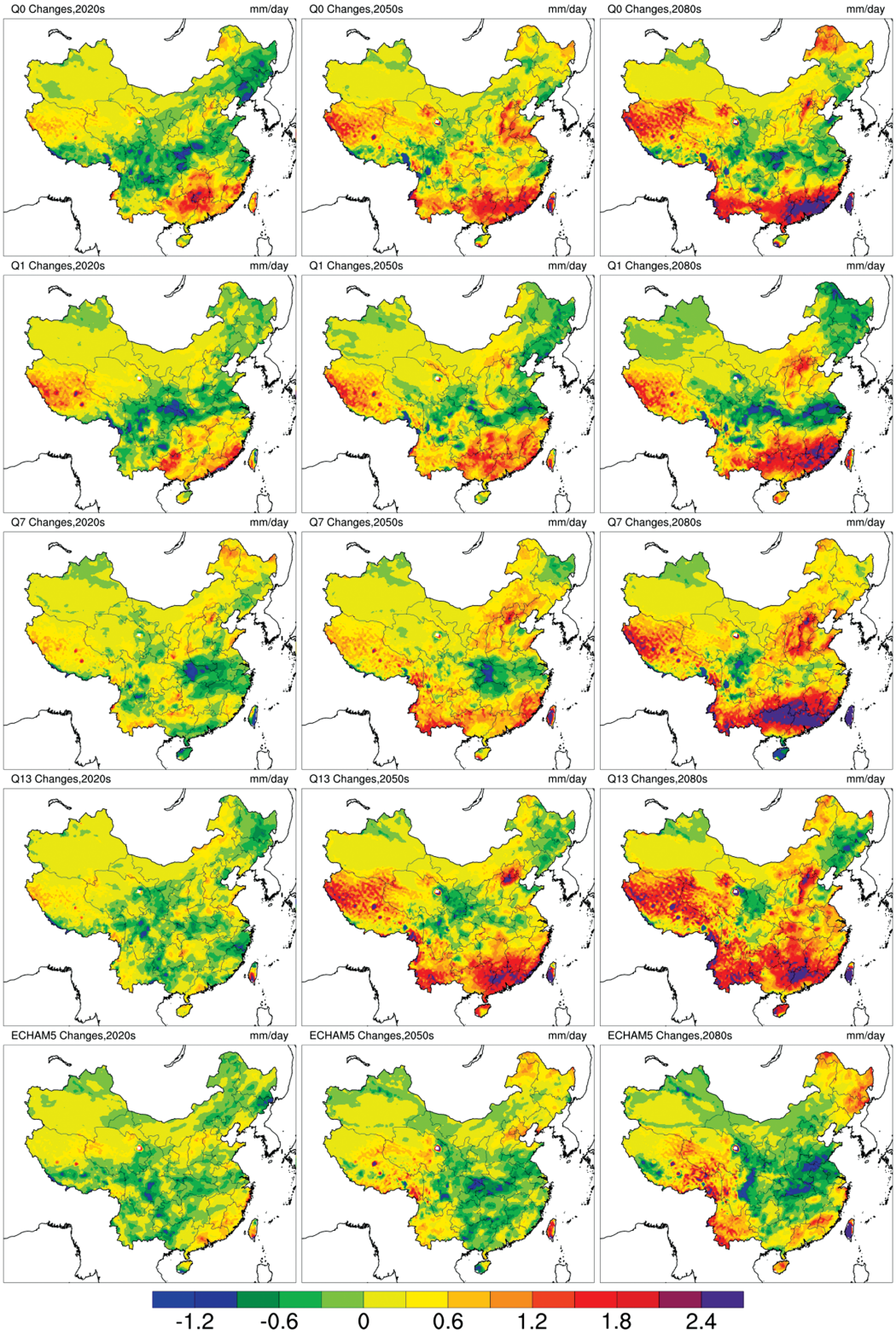

Figure 12. Projected patterns of precipitation changes (mm/d) for JJA over China in future. Each row represents an RCM member and from top to bottom these are Q0, Q1, Q7, Q13, and ECHAM5. Each column represents a period. From left to right these are 2020s, 2050s, and 2080s.

AGU Earth's Future

10.1002/2016EF000433

Table 2. Annual and Seasonal Mean Precipitation Changes in Future (mm/d)

		Winter			Spring			Summer			Autumn			Annual		
Regions	Ensembles	2020s	2050s	2080s	2020s	2050s	2080s	2020s	2050s	2080s	2020s	2050s	2080s	2020s	2050s	2080s
China	Q0	−0.012	0.137	0.156	0.037	0.187	0.339	0.110	0.396	0.573	0.059	0.210	0.322	0.048	0.226	0.353
	Q1	0.005	0.073	0.228	0.181	0.272	0.391	0.131	0.234	0.261	0.005	0.058	0.241	0.080	0.149	0.284
	Q7	0.118	0.147	0.209	0.146	0.248	0.427	0.189	0.409	0.694	0.064	0.206	0.278	0.129	0.253	0.407
	Q13	0.093	0.182	0.299	0.151	0.332	0.518	0.135	0.545	0.829	0.031	0.221	0.345	0.102	0.320	0.498
	ECHAM5	0.012	0.049	0.116	0.085	0.199	0.278	0.030	0.209	0.309	−0.011	0.132	0.291	0.029	0.140	0.259
	Average	**0.043**	**0.118**	**0.202**	0.120	0.248	0.391	**0.119**	**0.359**	**0.533**	0.030	0.165	0.295	**0.078**	**0.218**	**0.360**
NE	Q0	0.050	0.097	0.204	0.019	0.133	0.197	**−0.110**	0.213	0.368	0.131	0.185	0.226	0.022	0.150	0.254
	Q1	0.055	0.128	0.221	0.217	0.268	0.173	**−0.093**	−0.136	−0.312	0.134	0.064	0.349	0.078	0.069	0.112
	Q7	0.063	0.076	0.195	0.197	0.247	0.342	**0.315**	0.327	0.404	0.096	0.198	0.185	0.168	0.212	0.286
	Q13	0.094	0.135	0.207	−0.072	0.141	0.199	**−0.034**	0.056	0.140	0.003	0.128	0.391	−0.002	0.115	0.234
	ECHAM5	0.027	0.146	0.223	0.144	0.221	0.372	**−0.143**	0.349	0.453	−0.031	0.021	0.147	−0.001	0.177	0.308
	Average	0.058	0.116	0.210	0.101	0.202	0.257	**−0.013**	0.162	0.211	0.067	0.119	0.260	0.053	0.145	0.239
N	Q0	0.121	0.417	0.281	0.234	0.423	0.548	0.021	0.465	0.258	0.146	0.207	0.574	0.130	0.373	0.419
	Q1	−0.013	0.062	0.134	0.206	0.391	0.367	0.016	0.111	0.502	−0.163	−0.034	0.328	0.011	0.124	0.337
	Q7	0.217	0.242	0.294	0.293	0.419	0.339	0.233	0.485	0.824	0.103	0.265	0.128	0.212	0.353	0.400
	Q13	0.071	0.113	0.462	0.259	0.318	0.497	0.046	0.235	0.390	−0.095	0.093	0.088	0.070	0.190	0.359
	ECHAM5	0.028	0.097	0.268	0.148	0.164	0.091	0.163	0.105	−0.221	0.093	0.299	0.464	0.108	0.162	0.156
	Average	0.085	0.186	0.288	**0.228**	0.343	0.368	0.096	0.280	0.351	0.017	0.166	0.316	0.106	0.240	0.334
SE	Q0	**−0.211**	0.289	0.235	0.115	0.404	0.994	0.272	0.661	0.515	**−0.052**	0.174	0.307	0.031	0.376	0.517
	Q1	**−0.334**	0.001	0.639	0.079	0.354	1.018	0.228	0.453	0.547	**−0.454**	−0.254	0.061	−0.120	0.130	0.569
	Q7	**0.253**	0.288	0.367	0.188	0.463	0.943	−0.096	0.227	1.145	**−0.221**	0.053	0.064	0.031	0.258	0.634
	Q13	**0.129**	0.576	0.912	0.648	1.183	**1.663**	−0.061	0.770	1.138	**−0.114**	0.224	0.139	0.150	0.689	0.963
	ECHAM5	**0.008**	0.098	0.154	0.044	0.568	0.682	0.005	−0.275	−0.081	**−0.206**	0.053	0.054	−0.037	0.100	0.211
	Average	**−0.031**	0.250	0.461	0.215	0.594	1.060	0.070	0.367	0.653	**−0.209**	0.050	0.125	0.011	0.311	0.579

AGU Earth's Future

10.1002/2016EF000433

Table 2. (continued)

		Winter			Spring			Summer			Autumn			Annual		
Regions	Ensembles	2020s	2050s	2080s	2020s	2050s	2080s	2020s	2050s	2080s	2020s	2050s	2080s	2020s	2050s	2080s
W	Q0	−0.009	0.074	0.101	−0.011	0.109	0.091	0.203	0.565	0.757	0.135	0.313	0.359	0.079	0.258	0.332
	Q1	0.051	0.012	0.177	0.057	0.160	0.191	0.475	0.454	0.391	0.080	0.126	0.233	0.166	0.177	0.252
	Q7	0.111	0.113	0.145	0.146	0.197	0.238	0.343	0.502	0.808	0.077	0.108	0.375	0.169	0.230	0.396
	Q13	0.038	0.095	0.187	0.302	0.308	0.513	0.235	0.835	1.264	0.085	0.243	0.468	0.165	0.370	0.608
	ECHAM5	0.041	−0.043	0.004	0.016	0.110	0.012	0.049	0.342	0.561	0.154	0.217	0.313	0.065	0.151	0.232
	Average	0.046	0.050	0.123	0.102	0.177	0.209	0.261	0.540	0.756	0.106	0.201	0.350	0.129	0.237	0.364
NW	Q0	0.032	0.073	0.098	0.064	0.121	0.150	0.051	0.119	0.186	0.029	−0.008	0.025	0.044	0.076	0.115
	Q1	0.071	0.055	0.080	0.092	0.046	0.112	0.033	0.035	0.017	−0.008	−0.018	0.006	0.047	0.030	0.054
	Q7	0.043	0.074	0.119	0.030	0.068	0.140	0.035	0.065	0.077	0.019	0.016	0.022	0.032	0.056	0.090
	Q13	0.043	0.066	0.118	0.125	0.154	0.219	0.068	0.154	0.182	0.075	0.037	0.043	0.078	0.103	0.141
	ECHAM5	0.026	0.105	0.143	0.100	0.097	0.171	0.033	0.006	0.012	0.016	0.059	0.068	0.044	0.066	0.099
	Average	0.043	0.075	0.112	0.082	0.097	0.158	0.044	0.076	0.095	**0.026**	**0.017**	**0.033**	**0.049**	**0.066**	**0.100**

The pattern of precipitation changes in spring in the 2020s shows a similar distribution to that in winter. However, precipitation is likely to have a reducing intention over the northeast, Sichuan Basin, and southern Tibet. In the middle of the century, the trend seems to move eastward to broader areas, such as Jiangsu and Zhejiang in Q1 and Q7. But even negative changes, it appears that the whole of China would receive more precipitation in the long run till the end of the century. In summer, it is clear that there is a decreased precipitation belt along the northeast to southwest and the highest decrease center is located in the Chongqing and Hubei sections in the 2020s. Afterward, precipitation begins to increase gradually, especially in the south with changes from 0.367 mm/d in 2050s to 0.653 mm/d in the 2080s. In addition, the QUMP ensemble and ECHAM5 model have different opinions on future precipitation changes in the north. For example, there are obvious increasing trends with time in the four QUMP models, which is opposite to the ECHAM5 (decrease ~ 0.22 mm/d in 2080s relative to the baseline period). Unlike the first three seasons, Figure 13 shows the distinct probability distributions for the next three periods in autumn, in which the variation range of precipitation is relatively smaller. Furthermore, the rainfall in many areas even shows a declining trend in the 2020s, which is obvious across the southeast (a particular decrease of ~0.2 mm/d). Nevertheless, the overall change trend in precipitation is evidently positive from the beginning to the middle century.

Figure 14 show maps projecting minimum, maximum, and average annual precipitation of all grid cells over China in the next three periods. The results clearly show that the future wet centers are located in the southeast and southern Tibet and the dry center appears in the northwest with little changes relative to the baseline period. The outcomes of averaged annual precipitation in different period also present future precipitation will be increasing over time, especially in the southeast (i.e., 6–7 mm/d). By comparing the minimum and maximum map of each period, there is a wider gap between them over southeast China and northwest Tibet, indicating that most significant uncertainties are likely to exist in these regions. As mentioned earlier, the reasons for this lie in many aspects and one may be due to the intrinsic limitations of boundary data in RCMs, which cannot fairly reflect local or regional climatic characterizations.

In summary, the annual mean precipitation in China is projected to remain on an overall growth trend in the long term, most likely averaging at the rate about 0.15 mm/d per period, even though some regions or seasons show a slightly decreased trend in the early years of this century (i.e., decreasing 0.209 mm over the southeast during autumn). The changes in magnitude of precipitation are larger in summer and smaller in winter and autumn, which means China will be in a wetter scenario during the traditional rainy seasons. In addition, despite similar signs for all seasons in China, QUMP models project general wetter conditions compared with the ECHAM5.

The annual cycles of mean precipitation changes in three future periods for China and five subregions are shown in Figure 15. In order to further explore the uncertainties involved in the probabilistic projections of precipitation, we plot the five models together to form a variation trend band, whose width indicates the spread of precipitation change. In the future, the precipitation presents obvious spatial and temporal variations and characteristics. The amplitude of precipitation changes is more in wetter regions (i.e., southeast) and warmer months (i.e., May–August). Specifically, the changes of monthly mean precipitation show mixed signs, with a maximum increase as high as 1.6 mm/d and a minimum decrease of about −0.8 mm/d in other months (i.e., May and September), as compared to the simulated baseline over China. Similarly, the performances of the five predefined areas are not in complete accord with future precipitation. For example, the precipitation variation trend is projected to exceed 1.0 mm/d in June in the northeast, but is followed by a sharp drop below ~−1.2 mm/d in August, while in September it is likely to be positive again (~0.8 mm/d). The northern projected tendency is to fluctuate between positive and negative, peaking in July (~2.0 mm/d, but delayed with time) and the minimum in June (~−2.0 mm/d). In addition, although the total rainfall is increasing in the beginning of this century over the southeast, there are some uncertainties or ambiguities for the trend in the middle of this century, when rainfall is likely to decrease in May and winter months but tends to increase in other months. In the far western region and the dry northwest of China, the extent of variation in precipitation is relatively small, owing to the essential shortage of water in these areas. However, the future trend in the west exhibits a pronounced discrepancy from July to September in the 2050s.

Generally speaking, the results suggest that the projected range for precipitation is apparently wider in the 2050s and 2080s as compared to the initial period of 2020s, which shows that there are large disagreements

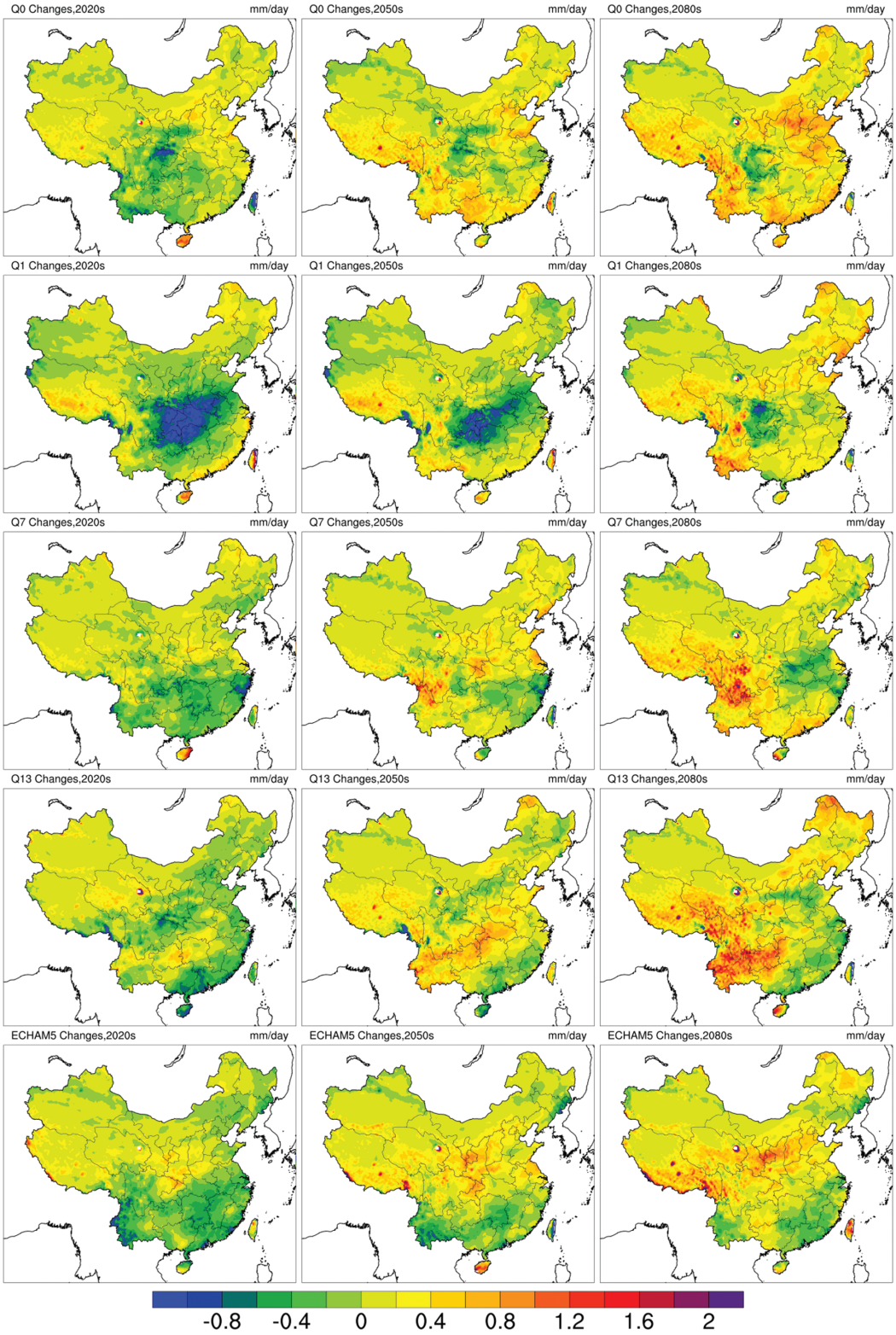

Figure 13. Projected patterns of precipitation changes (mm/d) for SON over China in future. Each row represents an RCM member and from top to bottom these are Q0, Q1, Q7, Q13, and ECHAM5. Each column represents a period. From left to right these are 2020s, 2050s, and 2080s.

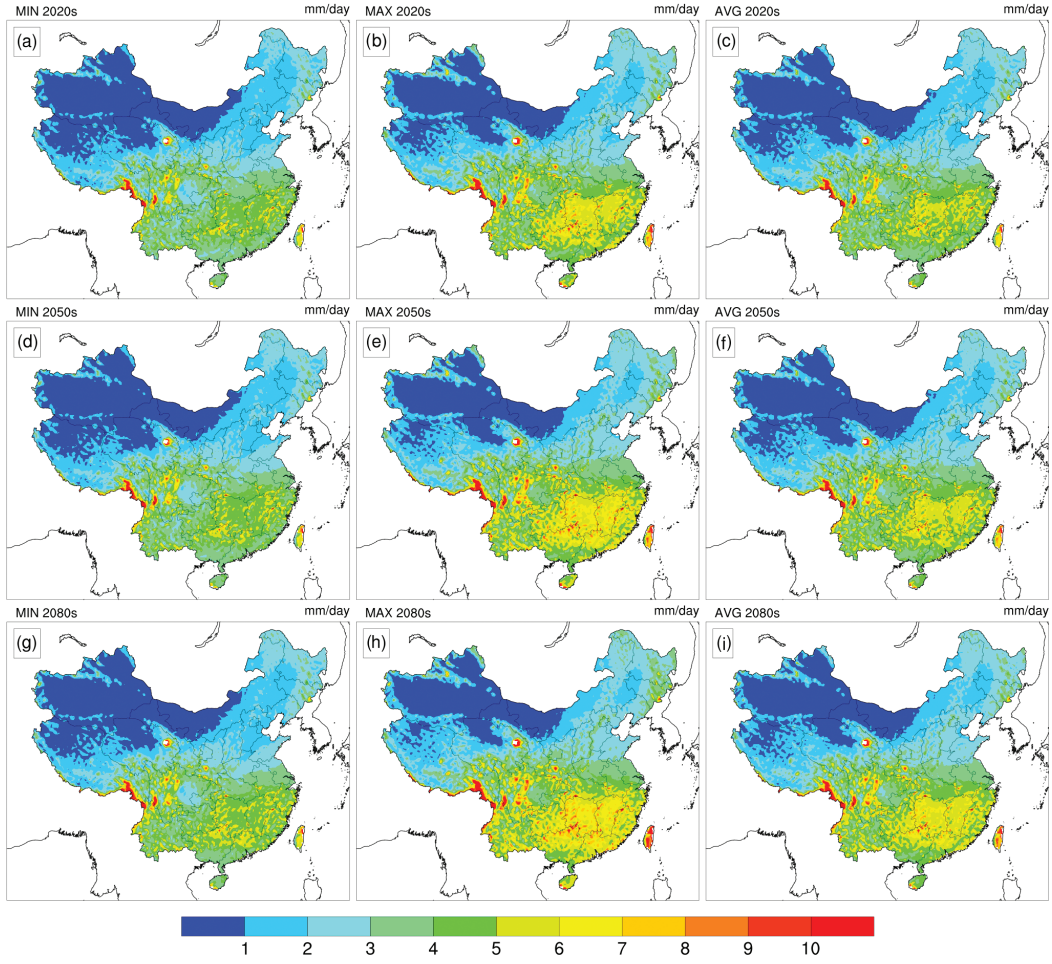

Figure 14. Projected patterns of annual precipitation changes (mm/d) over China in future. Each row represents the minimum, maximum, and average projection for all grids respectively. Each column represents a period. From left to right these are 2020s, 2050s, and 2080s.

among the models for mid-and-long term projections. Likewise, in each period the same holds true for rainy seasons (i.e., from June to September) compared with dry seasons.

4. Conclusions

In this study, we conducted a long continuous simulation (1949–2100) of precipitation over China through the PRECIS regional climate modeling system with a 25-km horizontal resolution. To evaluate the model's performance for historical simulation and investigate future probable ranges of precipitation, a set of lateral boundary conditions, including four QUMP members from a HadCM3-based perturbed-physics ensemble and the ECHAM5 model, are employed to drive the PRECIS model for generating high-resolution ensemble projections of precipitation over China.

Overall, the performance of PRECIS is reasonable in the simulation of spatial precipitation distribution when compared with corresponding observations from the APHRODITE project dataset in the baseline period (1961–1990). In detail, the well performance of PRECIS is demonstrated by high spatial pattern correlations with observations and small RMSE values. Nevertheless, wet or dry biases still exist in some local regions. For example, the PRECIS ensemble is likely to overestimate precipitation in the south and tends to present slightly dry biases in the northwest and southeast coasts of China, especially in the first half a year in the annual cycle. Additionally, relatively large biases appear in the west and the rainy seasons (i.e., from May to September), implying that geographical location and sufficient water vapor supply may play vital roles in the precipitation simulations. The possible reason for the large uncertainties in the northwest and west

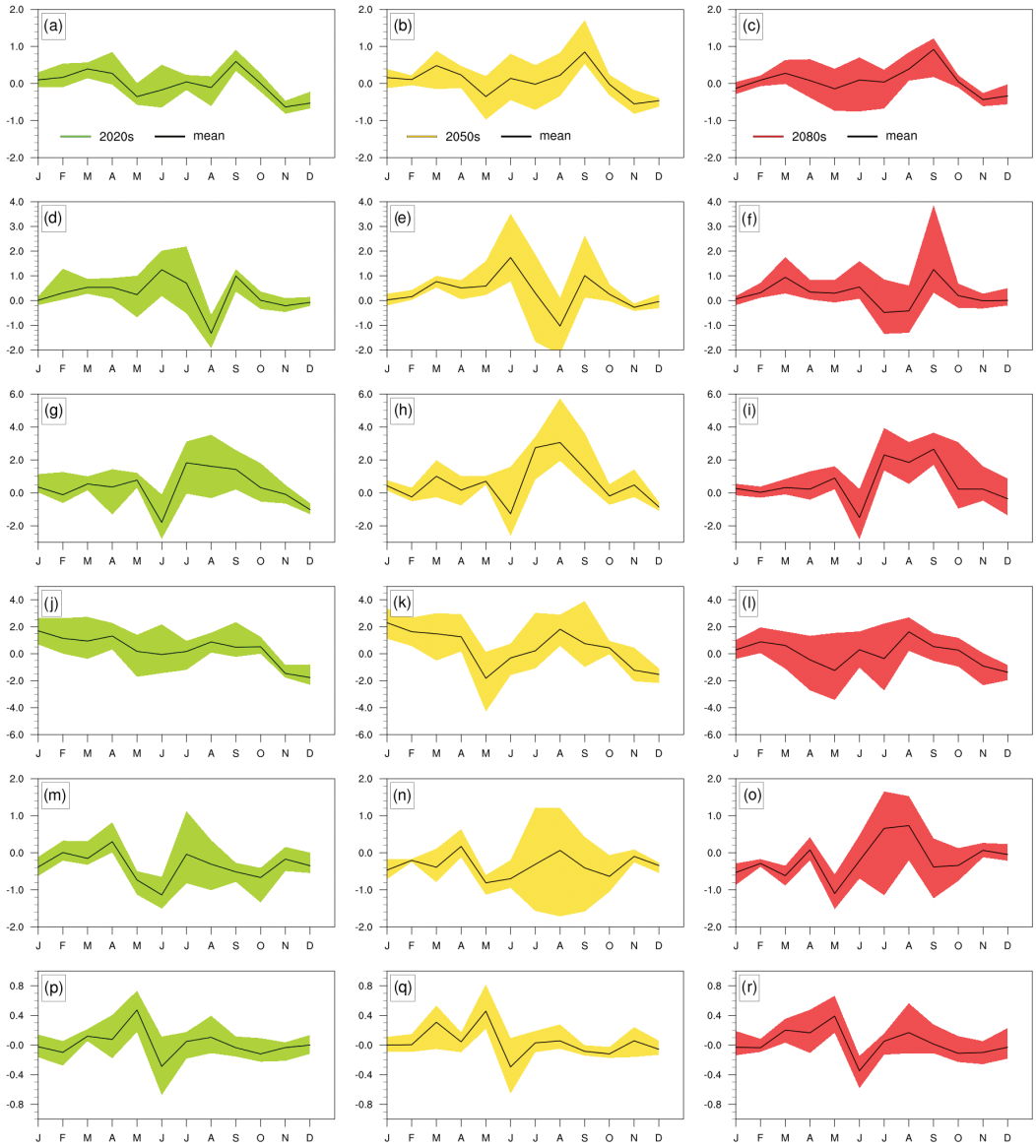

Figure 15. Annual cycles of mean precipitation changes over the whole China and five subregions. The columns from left to right represent the period 2020s (green band), 2050s (yellow band), and 2080s (red band), respectively. The rows represent different regions, namely, (a–c) for China, (d–f) for NE, (g–i) for N, (j–l) for SE, (m–o) for W, and (p–r) for NW. The black solid line is average value for the ensemble.

might be deficiencies of GCM boundary conditions in reflecting these mountainous or isolated regions, along with inevitable observational errors.

Future changes in precipitation over China as predicted by PRECIS for three successive 30-year periods (i.e., 2020s, 2050s, and 2080s) in the 21st century are further analyzed in this study. It is shown that annual mean precipitation over China is likely to increase throughout the 21st century (i.e., by 0.078 mm/d in 2020s, 0.218 mm/d in 2050s, and 0.360 mm/d in 2080s), although some model results present a slightly decreased trend for certain regions (i.e., southeast) or seasons (i.e., autumn) in the early years of this century. Apparent spatial and temporal variations are also reported in the projected precipitations from the PRECIS ensemble. For example, bigger changes in precipitation are usually observed in summer; projected precipitation changes in the southeast are apparently higher than other regions. By analyzing the precipitation changes in the annual cycle, the fluctuation range of the ensemble simulations will increase with time periods from 2020s to 2080s, indicating that the longer the projecting periods, the more uncertain the projections will be.

Acknowledgments
This research was supported by the Natural Sciences Foundation (51190095, 51225904), the Program for Innovative Research Team in University (IRT1127), the 111 Project (B14008), the National Basic Research Program (2013CB430401), the Natural Science, and Engineering Research Council of Canada, National Key Research and Development Plan (2016YFA0601502 and 2016YFC0502800).

References

Adger, W. N., N. W. Arnell, and E. L. Tompkins (2005), Successful adaptation to climate change across scales, *Global Environ. Chang.*, *15*, 77–86, doi:10.1016/j.gloenvcha.2004.12.005.

Buontempo, C., C. Mathison, R. Jones, K. Williams, C. Wang, and C. Mcsweeney (2014), An ensemble climate projection for Africa, *Clim. Dyn.*, *44*, 1–22, doi:10.1007/s00382-014-2286-2.

Baker-Austin, C., C. J. A. Campos, A. Turner, W. A. Higman, and D. Lees (2013), Impacts of climate change on human health, *MCCIP Sci. Rev.*, *2013*, 257–262, doi:10.14465/2013.arc27.257-262.

Carvalho, A. C., A. Carvalho, H. Martins, C. Marques, A. Rocha, C. Borrego, D. X. Viegas, and A. I. Miranda (2011), Fire weather risk assessment under climate change using a dynamical downscaling approach, *Environ. Model. Softw.*, *26*, 1123–1133, doi:10.1016/j.envsoft.2011.03.012.

Centella-Artola, A., M. A. Taylor, A. Bezanilla-Morlot, D. Martinez-Castro, J. D. Campbell, T. S. Stephenson, and A. Vichot (2014), Assessing the effect of domain size over the Caribbean region using the PRECIS regional climate model, *Clim. Dyn.*, *44*, 1901–1918, doi:10.1007/s00382-014-2272-8.

Gagnon, S., B. Singh, J. Rousselle, and L. Roy (2005), An Application of the Statistical DownScaling Model (SDSM) to Simulate Climatic Data for Streamflow Modelling in *Québec. Can. Water Resour. J.*, *30*, 297–314.

Hughes L. (2000) Biological consequences of global warming: is the signal already apparent? Trends *Ecol. Evol.*, *15*, 56–61, doi:10.1016/S0169-5347(99)01764-4.

Jiang, T., Z. W. Kundzewicz, and B. Su (2008), Changes in monthly precipitation and flood hazard in the Yangtze River Basin, China, *Int. J. Climatol.*, *28*, 1471–1481, doi:10.1002/joc.1635.

Jones, R. G., M. Noguer, D. C. Hassell, D. Hudson, S. S. Wilson, G. J. Jenkins, and J. F. B. Mitchell (2004), *Generating High Resolution Climate Change Scenarios Using PRECIS* , pp. 40 , Met Office Hadley Cent., Exeter.

Kong, X., S. Dorling, and R. Smith (2011), Soil moisture modelling and validation at an agricultural site in Norfolk using the Met Office surface exchange scheme (MOSES), *Meteorol. Appl.*, *18*, 18–27, doi:10.1002/met.197.

Li, P. (1996), The Arctic Sea ice and climate change, *J. Glaciol. Geocryol.*, *18*(1), 72–80.

Liu, Y., and K. Fan (2013), A new statistical downscaling model for autumn precipitation in China, *Int. J. Climatol.*, *33*, 1321–1336, doi:10.1002/joc.3514.

Liu, S., W. Gao, and X. Z. Liang (2013), A regional climate model downscaling projection of China future climate change, *Clim. Dyn.*, *41*, 1871–1884, doi:10.1007/s00382-012-1632-5.

Lu, X. X., and L. Ran (2011), China flood havoc highlights poor urban planning, *Nat. Hazards*, *56*, 575–576, doi:10.1007/s11069-011-9720-0.

Luo, L., W. Tang, Z. Lin, and E. F. Wood (2013), Evaluation of summer temperature and precipitation predictions from NCEP CFSv2 retrospective forecast over China, *Clim. Dyn.*, *41*, 2213–2230, doi:10.1007/s00382-013-1927-1.

Meehl, G. A., C. Tebaldi, G. Walton, D. Easterling, and L. Mcdaniel (2009), Relative increase of record high maximum temperatures compared to record low minimum temperatures in the U.S, *Geophys. Res. Lett.*, *36*, 110–125, doi:10.1029/2009GL040736.

Min, S. K., X. Zhang, F. W. Zwiers, and G. C. Hegerl (2011), Human contribution to more-intense precipitation extremes, *Nature*, *470*, 378–381, doi:10.1038/nature09763.

Qiu, J. (2010), China drought highlights future climate threats, *Nature*, *465*, 142–143, doi:10.1038/465142a.

Root, T. L., J. T. Price, K. R. Hall, S. H. Schneider, C. Rosenzweig, and J. A. Pounds (2003), Fingerprints of global warming on wild animals and plants. *Nature 421*, 57–60, doi:10.1038/nature01309.

Shen, C., W. C. Wang, G. Wei, and Z. Hao (2006), A pacific decadal oscillation record since 1470 AD reconstructed from proxy data of summer rainfall over Eastern China, *Geophys. Res. Lett.*, *33*, 279–296, doi:10.1029/2005GL024804.

Trenberth, K. E., and J. T. Fasullo (2012), Climate extremes and climate change: The Russian heat wave and other climate extremes of 2010, *J. Geophys. Res. Atmos.*, *117*, 127–135, doi:10.1029/2012JD018020.

Wang, X., G. Huang, Q. Lin, X. Nie, G. Cheng, Y. Fan, Z. Li, Y. Yao, and M. Suo (2013), A stepwise cluster analysis approach for downscaled climate projection – A Canadian case study, *Environ. Model. Softw.*, *49*, 141–151, doi:10.1016/j.envsoft.2013.08.006.

Wang, X., G. Huang, and J. Liu (2014a), Projected increases in intensity and frequency of rainfall extremes through a regional climate modeling approach, *J. Geophys. Res. Atmos.*, *119*, 13, doi:10.1002/2014JD022564.

Wang, X., G. Huang, and J. Liu (2014b), Projected increases in near-surface air temperature over Ontario, Canada: A regional climate modeling approach, *Clim. Dyn.*, *188*, 1–13, doi:10.1007/s00382-014-2387-y.

Wang, X., G. Huang, and J. Liu (2015), Twenty-first century probabilistic projections of precipitation over Ontario, Canada through a regional climate model ensemble, *Clim. Dyn.*, *46*, 1–23, doi:10.1007/s00382-015-2816-6.

Wang, X., G. Huang, and B. W. Baetz (2016), Dynamically-downscaled probabilistic projections of precipitation changes: A Canadian case study, *Environ. Res.*, *148*, 86–101, doi:10.1016/j.envres.2016.03.019.

Wetterhall, F., A. Bárdossy, D. Chen, S. Halldin, and C. Y. Xu (2006), Daily precipitation-downscaling techniques in three Chinese regions, *Water Resour. Res.*, *42*, 2526–2528, doi:10.1029/2005WR004573.

Williams, K., J. Chamberlain, C. Buontempo, and C. Bain (2015), Regional climate model performance in the Lake Victoria basin, *Clim. Dyn.*, *44*, 1699–1713, doi:10.1007/s00382-014-2201-x.

Yu, F., Z. Chen, X. Ren, and G. Yang (2009), Analysis of historical floods on the Yangtze River, China: Characteristics and explanations, *Geomorphology*, *113*, 210–216, doi:10.1016/j.geomorph.2009.03.008.

En-Tao, Y. U., H. J. Wang, and J. Q. Sun (2010), A quick report on a dynamical downscaling simulation over China using the nested model, *Atmos. Ocean. Sci. Lett.*, *3*, 325–329, doi:10.1080/16742834.2010.11446886.

Yu, E., J. Sun, H. Chen, and W. Xiang (2014), Evaluation of a high-resolution historical simulation over China: Climatology and extremes, *Clim. Dyn.*, *45*, 1–19, doi:10.1007/s00382-014-2452-6.

Zhang X, and Yan X (2015), A new statistical precipitation downscaling method with Bayesian model averaging: a case study in China. *Clim. Dyn.*, *45*, 1–15, doi:10.1007/s00382-015-2491-7.

Zhang, W., F. F. Jin, and A. Turner (2014), Increasing autumn drought over Southern China associated with ENSO Regime Shift, *Geophys. Res. Lett.*, *41*, 4020–4026, doi:10.1002/2014GL060130.